Using wavelets to characterize the wettability of porous materials

V. Sygouni,[1,2] C. D. Tsakiroglou,[1,*] and A. C. Payatakes[1,2]

[1]*Institute of Chemical Engineering and High Temperature Chemical Processes, Foundation for Research and Technology Hellas, Stadiou Street, Platani, P. O. Box 1414, GR-26504 Patras, Greece*

[2]*Department of Chemical Engineering, University of Patras, GR-26500 Patras, Greece*

(Received 18 April 2007; revised manuscript received 10 September 2007; published 9 November 2007)

Visualization experiments of rate-controlled immiscible displacement of oil by water are performed on a model porous medium of controlled fractional wettability, fabricated by mixing water-wet glass microspheres with strongly oil-wet polytetrafluoroethylene microspheres and packing them between two transparent glass plates. The growth pattern is video recorded and the transient response of the pressure drop across the pore network is measured for various fractions of oil-wet particles. The space-averaged capillary pressure coincides to the pressure drop measured across the porous medium. The oscillating transient signal of the capillary pressure is analyzed with multilevel wavelets to produce the best level wavelet details or best level capillary pressure spectrum (BLCPS) by minimizing the "entropy" of wavelet approximation. Invasion of water in oil-wet areas is reflected in high-frequency and low-amplitude fluctuations of the BLCPS. Correspondingly, invasion of water in water-wet areas is associated with low-frequency and high-amplitude fluctuations of the BLCPS. The displacement growth pattern is reflected in the "energy" and "frequency" of the BLCPS which along with the time-averaged capillary pressure are correlated with two parameters quantifying the spatial variation of wettability over the porous medium: the frontal wettability of the active interface of the fluids before each invasion step and the regional wettability of the area invaded by the displacing fluid.

DOI: 10.1103/PhysRevE.76.056304 PACS number(s): 47.55.nb, 68.08.Bc, 47.56.+r

I. INTRODUCTION

One of the key factors affecting multiphase flow processes in porous materials is the wettability of the internal surface of pores. In general, a surface may be termed as hydrophilic (water wet) or hydrophobic (oil wet, water repellent) with respect to an oil (gas)–water system, depending on its preference to attach water or oil (gas) molecules [1]. Much attention has been paid in the past on the elucidation of the role of wettability for enhanced oil and gas recovery processes from reservoir rocks and CO_2 storage in depleted oil reservoirs and deep saline aquifers [2–9]. Moreover, wettability is of primary importance for multiphase transport in a wide variety of synthetic porous materials such as filters, column packs, fuel cells, bio-materials, etc. [10–14]. Attention should be paid to soil wettability as it affects the spreading of organic pollutants in the subsurface and the efficiency of remediation technologies [15,16]. Moreover, it is worth noting that soil hydrophobicity is responsible for inhibited plant growth, reduced rainfall water infiltration, increased overland flow of water and soil erosion, uneven spatial and vertical wetting patterns, reduced evaporation, and enhanced risk of groundwater pollution [17,18]. The wettability of a pore surface is decided by the interaction of a great variety of microscopic parameters (pore geometry, surface chemical composition, *p*H, salinity, fluid system, history of fluid transport and reaction proceses, etc.) [1] and is reflected in the efficiency of two-phase flow processes and relevant macroscopic multiphase flow coefficients [8,19–21]. Based on such interrelationships, various methods have been suggested to characterize the wettability of reservoir rocks [19–23]. However, in all these methods it is very difficult and cumbersome to decouple the wettability from the pore structure effects on the measured variables. Moreover, the majority of natural and synthetic porous materials may contain various types of solid surfaces that exhibit different wettability with respect to an oil (gas)–water system.

During crude oil migration in reservoir rocks, the potential deposition of asphaltenes on low curvature solid surfaces (e.g., inside large pores or pore bodies) and the retention of formation water around high-curvature solid surfaces (e.g., inside small pores, pore corners, pore-wall roughness) may result in a mixed-wet system where hydrophilic and hydrophobic surfaces coexist at the pore scale [7]. Because of the soil heterogeneity, the preferential flow of liquid organic wastes through highly permeable pathways and the subsequent adsorption of organic molecules on soil grains may increase locally the soil organic matter, thus creating fractional-wet conditions, where an oil-wet cluster of pores spans an otherwise water-wet pore network [24]. Soil hydrophobicity may also be caused by a coating of waxlike substances (long-chained organic molecules) on individual soil particles [17,18]. These substances may be released from a range of plants, decaying organic matter, soil fauna and micro-organisms either naturally or during burning (forest fires) [25]. Atomic force microscope images have revealed that fractional-wet conditions may be established, as the wax coating around soil particles are not continuous, but they form nanoscale globules that expand and shrink depending on water availability [26]. Regarding the polymer electrolyte membrane fuel cells (PEMFCs), liquid water may fill the pore network within the gas diffusion layer (GDL) support and decrease the effective diffusivity of oxygen through the layer. In order to facilitate the transport of oxygen to the catalyst layer, GDLs are typically coated with a nonwetting

*Corresponding author. FAX: 30 2610 965223. ctsakir@iceht.forth.gr

polymer, such as polytetrafluoroethylene (PTFE), to create hydrophobic surfaces and pores that remain free of water [13].

From the aforementioned examples, it becomes clear that fractional-wet and mixed-wet states are common in both natural and synthetic porous materials [2,10–14,27–31]. The spatial distribution of oil-wet and water-wet surfaces within a fractional-wet pore network is closely related to the creation of network spanning clusters of oil-wet and/or water-wet pores which may act as preferential flow paths through the porous medium [32]. The transient response of the pressure drop measured across a porous medium during slow and rate-controlled displacement experiments is a "fingerprint" of the flow pattern which is governed by the spatial variation of the pore structure properties and wettability [33,34]. Experiments on long cores along with stability analysis and high-accuracy numerical simulations have revealed that existing continuum models and equilibrium relative permeability can be used to simulate accurately not only stable flow regimes but also flows characterized by large-scale viscous instabilities [35]. However, in relatively small porous media, where the length of viscous fingers is comparable to or exceeds the length of the medium, and small-scale instabilities induced by capillarity are dominant, the continuum approach is unable to reproduce the transient flow pattern and mechanistic pore network simulators are commonly employed to simulate immiscible displacements [8,33,34].

Using wavelets to analyze the fluctuations of the pressure drop signal measured across a two-layer model porous medium of small dimensions (the numbers of pores along x and y directions are $N_{px} \approx 130$, $N_{py} \approx 80$), it was realized that the spectrum of wavelet details (or equivalently the capillary pressure spectrum) is correlated implicitly with the fractional wettability of the pore surface [36]. It was also found that the amplitudes of the peaks of the capillary pressure spectrum (CPS) arising from the first-level wavelet details of the capillary pressure signal have a quasilinear relationship with a local coefficient of fractional wettability, presuming that the same class of flow events is concerned [36]. Nevertheless, no robust method has yet been developed to allow us to correlate explicitly the spatial distribution of the fractional wettability with parameters that quantify the signal of the pressure drop. It is the goal of the present work to develop a robust method of wavelet analysis in order to correlate the energy and frequency of the best level wavelet details with the spatial variation of wettability over those zones of the pore system where the displacing fluid has invaded.

II. MATERIALS AND METHODS

Visualization displacement experiments are performed on a transparent model porous medium consisting of glass (water-wet) and PTFE (oil-wet) microspheres of identical size (R=0.75 mm), packed between two cover glass plates which are sealed with silicon rubber that holds the spheres [36]. The length of the pore network between the inlet and outlet ports is L_N=0.1 m, and its width is W_N=0.06 m. The pore space contained between a hexagonal sphere pack and two plates [Fig. 1(a)] can be regarded as a two-layer network

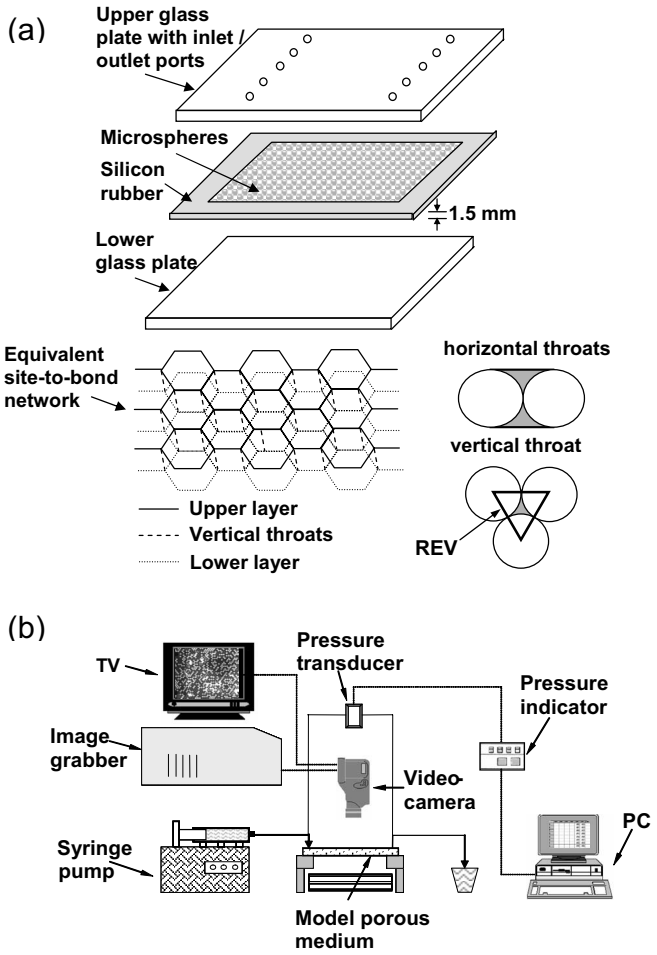

FIG. 1. (a) Model porous medium. (b) Experimental setup. (c) High-resolution snapshot of displacement.

of pore chambers (the void spaces left between one cover plate and three spheres touching each other) interconnected through throats (the narrow constrictions where the cross-sectional area is minimized) arranged in a triangular lattice, whereas vertical throats connect chambers of the upper layer with those of the lower one [Fig. 1(a)]. All pores are identical, the pore space is a three-dimensional (3D) periodic structure, and the representative elementary volume (REV) is a triangular prism [Fig. 1(a)]. Initially, the porous medium is filled with paraffin oil which is then displaced by water (primary imbibition) injected at a very low flow rate [Fig. 1(b), Table I]. The displacement growth pattern is video recorded [Fig. 1(c)] and the pressure drop across the porous medium is measured during each experiment. The fractional wettability of the porous medium is controlled by varying the fraction of

TABLE I. Physicochemical properties of POW system.

Density of paraffin oil[a] ρ_o (kg/m^3)	820
Viscosity of paraffin oil μ_o (Pa s)	0.026
Density of deionized water ρ_w (kg/m^3)	995
Viscosity of deionized water μ_w (Pa s)	10^{-3}
Interfacial tension γ_{ow} (Nt/m)	35.5×10^{-3}
Contact angle of water–paraffin oil on glass (deg)	20
Contact angle of water–paraffin oil on PTFE (deg)	178

[a]Merck product no. K34089774 502.

oil-wet spheres, ξ, and is reflected in the capillary behavior of the pore system [36]. It is well known that primary imbibition is rarely encountered in practical problems (e.g., oil reservoirs) and the coexistence of both fluids (oil-water or gas-water) is a more realistic situation. However, our goal is to examine the sensitivity of the measured variables (transient signal of the pressure drop) to the pore surface wettability throughout the entire porous medium. This sensitivity is enhanced when the pore space is fully occupied by oil, as the pore volume that is available to fluid redistribution (associated with fluctuations of the capillary pressure) is maximized.

A detailed description of the experimental setup and method of signal analysis for a fractional-wet pore system consisting of strongly oil-wet PTFE spheres and intermediate-wet glass spheres [silicon oil–water system (SOW)] has been reported elsewhere [36]. In the present work, a second fluid system paraffin oil–water (POW) is used so that the fractional-wet pore system is a mixture of strongly oil-wet and strongly water-wet spheres (Table I). The method used to analyze the pressure drop signals measured with the SOW fluid system [36] is unable to analyze the signals measured with POW fluid system. This is due to the small amplitude and low frequency of the most important fluctuations that are not detectable by the first-level wavelet analysis. Therefore, the signal analysis method was revised so as to become robust and independent of the contact angles.

III. CAPILLARY AND VISCOUS FORCES

The global capillary number Ca is defined by

$$\mathrm{Ca} = \mu_w u/\gamma_{ow}, \tag{1}$$

where μ_w is the water viscosity, u is the superficial flow velocity, and γ_{ow} is the oil-water interfacial tension. All experiments were performed at a low value of capillary number $\mathrm{Ca}=1.0\times10^{-8}$. In order to estimate the ratio of viscous to capillary forces at the pore and network scales, the microscopic Ca_P and macroscopic Ca_N capillary numbers are defined through the relations [36]

$$\mathrm{Ca}_P = \mathrm{Ca}\,\kappa\left(\frac{\langle r_H\rangle l_p}{k\cos\theta_e}\right) \tag{2}$$

and

TABLE II. Values of dimensionless numbers for POW fluid system.

Dimensionless number	POW system
Global capillary number Ca	1.01×10^{-8}
Microscopic capillary number Ca_p	65.4×10^{-6}
Macroscopic capillary number Ca_N	43×10^{-4}
Bond number	2×10^{-3}

$$\mathrm{Ca}_N = \mathrm{Ca}\,\kappa\left(\frac{\langle r_H\rangle L_N}{k\cos\theta_e}\right), \tag{3}$$

respectively, where $\langle r_H\rangle$ is an average equivalent hydraulic radius, l_p is the pore length, L_N is the length of the pore network, and $\kappa=\mu_o/\mu_w$ is the viscosity ratio [36]. The values of both aforementioned numbers are much less than 1.0 (Table II) indicating that capillary forces are dominant.

The pores formed between solid spheres have a converging-diverging shape, and concave solid-wall curvature. Even for contact angles smaller than 90° (water imbibition) the maximum equilibrium capillary pressure for a water-oil meniscus to penetrate into a pore is positive (the interfacial configuration is convex) and occurs downstream from the throat [36–38]. Depending on the contact angle or the fraction of oil-wet spheres, the critical normalized curvature $J^*=P_{c,\mathrm{crit}}R/\gamma_{ow}$ for meniscus penetration in a pore created between two spheres and one plate may range from 1 to 5 [36].

Before water breakthrough, the total pressure drop across a zone invaded by water, ΔP, can be regarded as equal to the sum of the hydrodynamic pressure drops across the invading water and noninvaded oil, ΔP_h, increased (or reduced) by a positive (or negative) macroscopic capillary pressure which depicts the menisci capillary pressures averaged along the front [34]. The detailed picture of a displacement dominated by small-scale instabilities (capillary fingering) is not cap-

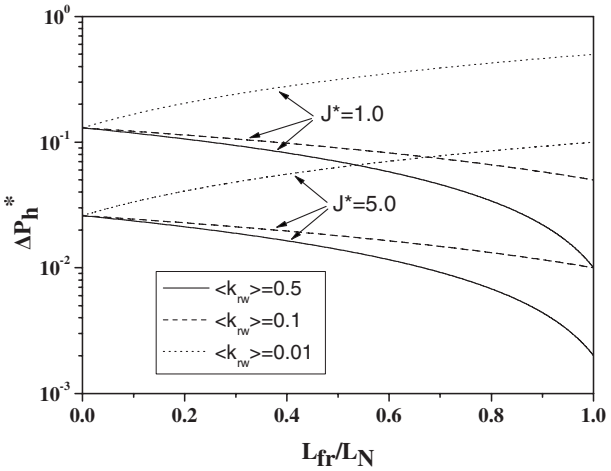

FIG. 2. Variation of the dimensionless hydrodynamic pressure drop as a function of the axial position of the displacement front for various values of the average water relative permeability and critical mean curvature of meniscus.

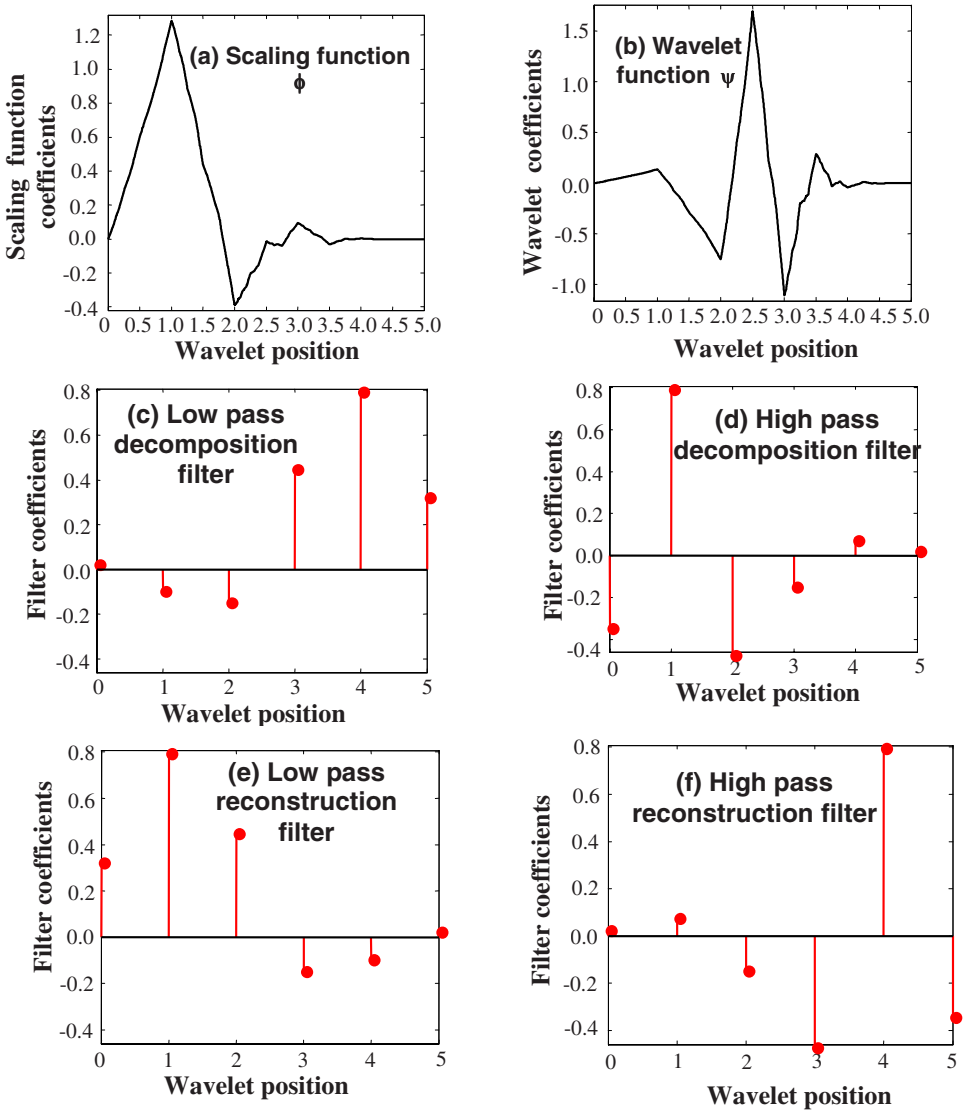

FIG. 3. (Color online) Wavelet db3: (a) scaling function φ, (b) db3 wavelet function ψ, (c) low-pass decomposition filter, (d) high-pass decomposition filter, (e) low-pass reconstruction filter, and (f) high-pass reconstruction filter.

tured by the macroscopic two-phase flow equations, and an invasion percolation or dynamic pore network simulator must be used [8,32–34]. Nevertheless, taking into account the integrated form of multiphase Darcy law and assuming that $k_{ro} \approx 1.0$, we get the approximate relation

$$\Delta P = \Delta P_h + \langle P_c \rangle \approx \frac{\mathrm{Ca}\ \gamma_{ow} L_N}{k}\left[\frac{L_{fr}}{L_N \langle k_{rw} \rangle} + \kappa\left(1 - \frac{L_{fr}}{L_N}\right)\right] + \langle P_c \rangle, \tag{4}$$

where L_{fr} is the axial position of the displacement front, and $\langle k_{rw} \rangle$ is the relative permeability of invading phase (water) averaged over the swept zone. The measured pressure drop across the network is a "fingerprint" of the flow pattern. At very low flow rates ($\mathrm{Ca} = 10^{-8}$), the macroscopic capillary pressure $\langle P_c \rangle$ may become comparable to or exceed the hydrodynamic term ΔP_h and the fluctuations of $\langle P_c \rangle$, arising from frontal menisci motion between unstable and stable positions of the pore space [34,36], are reflected in the measured ΔP. For an analysis of order of magnitude, a dimensionless viscous pressure drop ΔP_h^* is defined by

$$\Delta P_h^* = \frac{\Delta P_h}{P_{c,\mathrm{crit}}} = \frac{\mathrm{Ca}\ LR}{J^* k}\left[\frac{L_{fr}}{L_N \langle k_{rw} \rangle} + \kappa\left(1 - \frac{L_{fr}}{L_N}\right)\right]. \tag{5}$$

For the specific properties of the experimental model ($k = 1500 \times 10^{-12}$ m^2), as the displacement proceeds, ΔP_h^* may increase or decrease depending on the value of $\langle k_{rw} \rangle$, it is less than 0.1 and may increase substantially only when $\langle k_{rw} \rangle$ becomes very low (Fig. 2). In experiments, $\langle k_{rw} \rangle$ tends to a very low value after breakthrough, given that near the outlet, water saturation drops rapidly as water tends to escape through one or more thin threads connecting the invading fluid (bulk phase) with the outlet ports (capillary end effect). For this reason, any after-breakthrough data are excluded from the analysis.

Accounting for the negligible to small contribution of viscous forces to the pressure drop measured across the model porous medium at low flow rates, and the fact that wavelet analysis is focused on the quantification of the pressure drop fluctuations that are associated with changes of the spatially averaged capillary pressure, in the following, instead of using the term "pressure drop" we refer to "capillary pressure."

Of course this capillary pressure concerns rate-controlled experiments and should not be confused with the conventional capillary pressure commonly measured with pressure-controlled experiments (e.g., mercury injection, porous plate method, etc.).

IV. CONCEPTS FROM WAVELET ANALYSIS

An extensive presentation of the methodology used for the wavelet transform of a signal has been reported elsewhere [36] (Appendix A). Here, emphasis is placed on the energy and entropy of signals. In signal analysis theory, the energy E_s of a continuous time signal, $f(t)$, is given by [39]

$$E_s = \langle f(t), f(t) \rangle = \int_{-\infty}^{\infty} |f(t)|^2 dt. \tag{6}$$

The "signal energy" and the thermodynamic notion of energy are not exactly the same but they are interrelated, and it is possible to convert from one to the other by using the relation

$$E = \frac{E_s}{Z} = \frac{1}{Z} \int_{-\infty}^{\infty} |f(t)|^2 dt, \tag{7}$$

where Z represents the magnitude of the load driven by the signal. For example, if $f(t)$ represents the potential (in volts) of an electrical signal propagating across a transmission line, then Z would represent the characteristic impedance (in ohms) of the transmission line.

The signal energy can easily be calculated when a signal is transformed with Fourier or wavelet analysis based on the concept of the energy conservation (Appendix B). For orthonormal wavelet expansions, the conservation of energy in the wavelet domain is given by [40,41]

$$\sum_{j=0}^{j=N-1} f(j)^2 = \sum_{m=1}^{m=M} \sum_{i=0}^{i=(2^{M-m}-1)} [W^{(m)}(i)]^2, \tag{8}$$

where $f(x_j)$ is defined at N discrete points in time, and $W^{(m)}$ are the wavelet coefficients of scale m $[M=\log_2(N)]$. The total energy included in scale $R_m=2^m dy$ is calculated by summing the squared wavelet details at the scale m, namely [40,41],

$$T_E = N^{-1} \sum_{i=0}^{i=(2^{M-m}-1)} (W^{(m)}[i])^2. \tag{9}$$

Beyond the energy, a second thermodynamic notion, the "entropy," is used in signal analysis theory. The entropy quantifies the degree of uncertainty, or in other words, the lack of information in a system described by time series. Between other areas, the entropy is used in hydrology, geomorphology, and management of water resources [42]. If all information concerning a system is available, then its entropy is zero. Assuming a set of n events, the uncertainty relates to the determination of the event that will occur [42]. The definition of the entropy is given by Shannon [46]:

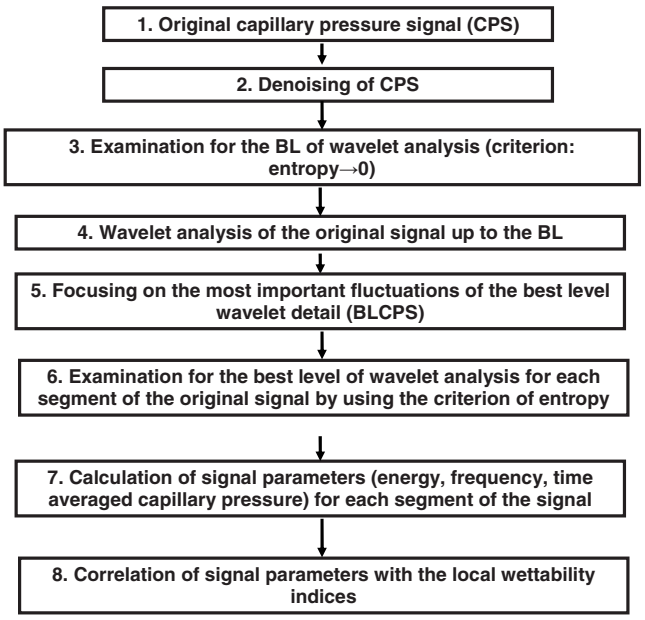

FIG. 4. Flow sheet of the method suggested to quantify continuous signals of pressure drop (capillary pressure) and correlate them with pore surface wettability.

$$S = H_1 = -\sum_{i=1}^{N} p_i \ln p_i, \tag{10}$$

where p_i is the probability that event i will occur, and assuming that $0 \ln 0 = 0$.

The wavelet entropy is minimized when the signal is characterized by an ordered behavior. Namely, when considering an ordered single frequency signal, the details of the multiresolution wavelet analysis is located around one scale or level. This level contains nearly 100% of the total signal energy, and the wavelet approximation entropy at this level is zero [42]. Therefore when analyzing one signal, its best level occurs when the wavelet approximation entropy is zero; then the wavelet detail contains most of the signal energy and no important signal information is lost. The entropy of a signal $f(t)$ in the wavelet domain is given by

$$E(f(t)) = -\sum_{i} f(t)_i [\ln f(t)_i]^2, \tag{11}$$

where $f(t)_i$ are the coefficients of $f(t)$ on an orthonormal base.

V. ANALYSIS OF CAPILLARY PRESSURE SIGNALS

A robust method was developed for the analysis of the capillary pressure signals in order to maximize the information that is transferred from the original signal to wavelet details (Figs. 4 and 5) by using orthonormal wavelets (Fig. 3).

The definition of entropy, Eq. (11), presumes that the capillary pressure values are smaller than unity. A dimensionless capillary pressure is defined according to

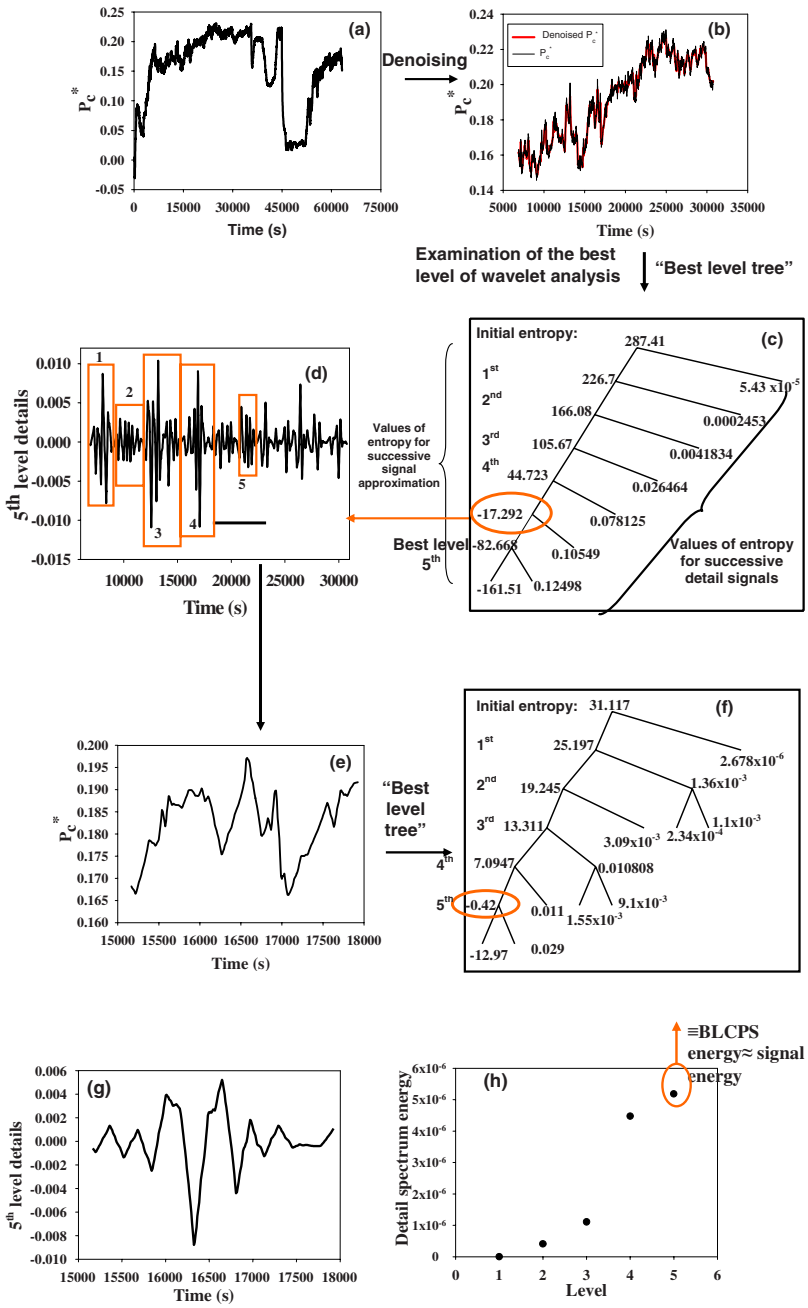

FIG. 5. (Color online) (a) Original signal of dimensionless capillary pressure. (b) A segment of the denoised signal of capillary pressure. (c) "Best-level tree:" entropy values of the wavelet approximations and details obtained at successive decomposition levels. (d) The best-level wavelet detail (fifth level) defines the best-level capillary pressure spectrum (BLCPS); the regions of BLCPS containing the most important detail fluctuations are outlined. (e) Magnification of the segment of denoised capillary pressure signal (b) that corresponds to region 4 of (d) (f) Best-level tree of the signal shown in (e). (g) BLCPS of the signal shown in (e). (h) Energy of wavelet detail from level 1 to level 5.

$$P_c^* = \frac{P_c}{P_{\max}}, \tag{12}$$

where

$$P_{\max} = \frac{8\gamma_{ow}}{R}. \tag{13}$$

γ_{ow} is the interfacial tension of the fluid system and R is the radius of microspheres. $P_{\max}$ is the critical capillary pressure required for a meniscus to penetrate into a cylindrical pore of diameter equal to that of the circle inscribed in the space between three spheres touching each other.

Initially, the signal of the dimensionless capillary pressure is denoised [Fig. 4, steps 1 and 2; Figs. 5(a) and 5(b)] by using Daubechie's "db3" wavelets (Fig. 3). The identification of the wavelet level is based on the multilevel decomposition of the signal to approximations and wavelet details and the calculation of the entropy of the successive approximations and details by using the wavelet toolbox of MATLAB. The best level occurs when the entropy of the approximation is very close to zero. This means that most of the signal energy is included in the wavelet details of this level and no important information is lost if the analysis stops at this level. When the best level is identified [Fig. 4, step 3, Fig. 5(c)], the wavelet details define the best level capillary pressure spectrum (BLCPS) containing the most important fluctuations of the original signal [Fig. 4, step 4, Fig. 5(d)]. The most important fluctuations of BLCPS [Fig. 5(d)] enable us to identify the corresponding fluctuations of the original capillary pressure signal at various locations [Fig. 4, step 5, Fig. 5(d)]. Each segment of the original capillary pressure

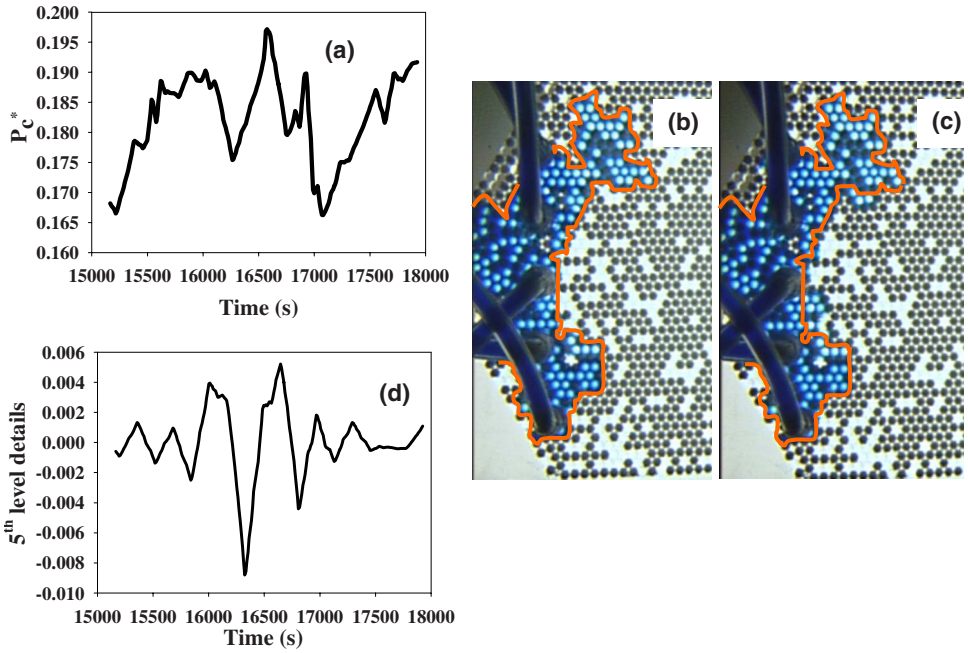

FIG. 6. (Color online) (a) Signal of dimensionless capillary pressure. (b) Snapshot of the displacement at the beginning of the signal; the water/oil interface (front) is outlined. (c) Snapshot of the displacement at the end of the signal; the new area that was occupied by the displacing fluid (water, dark color) is bounded between the old (outlined) and new position of the oil-water interface. (d) The BLCPS of the signal.

signal [e.g., segment no. 4, Fig. 5(e)] is reanalyzed up to its best level [Fig. 4, step 6, Fig. 5(f)] and the "signal energy" is calculated by using the BLCPS wavelet coefficients, Eq. (9) [Fig. 4, step 7, Figs. 5(g) and 5(h)]. The frequency of fluctuations in a segment of BLCPS is determined by dividing the number of the most important fluctuations to the corresponding time interval. The time-averaged capillary pressure of a segment of the original signal is calculated by averaging the dimensionless capillary pressure over the corresponding time interval. The video recorded images of the displacement allow us to quantify the wettability of the porous medium. The analyzed segment of the capillary pressure signal [Fig. 6(a)] can be attributed to the changes of the spatial fluid distribution, as shown in two successive images of the displacement growth pattern [Figs. 6(b) and 6(c)]. The first image [Fig. 6(b)] corresponds to the beginning of the capillary pressure signal [Fig. 6(a)] and the second one [Fig. 6(c)] corresponds to its end. Looking at the interface separating the two fluids before the invasion step, the frontal wettability is a quantitative measure of the wetting state of this interface and can be calculated by measuring the oil-wet and water-wet spheres of the water-oil interface

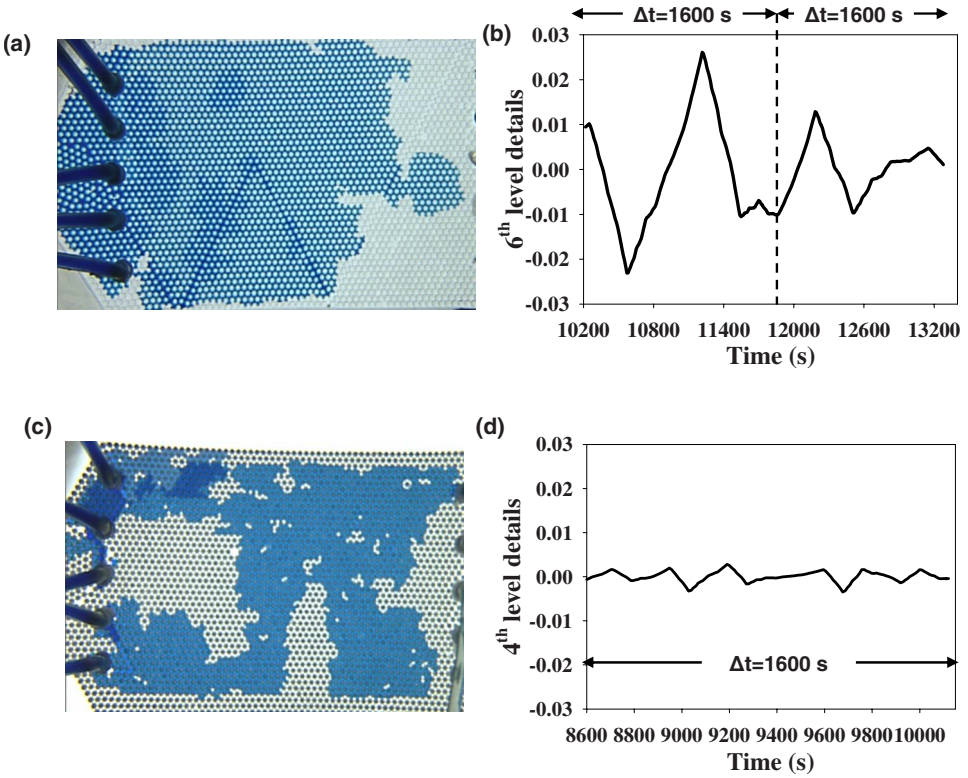

FIG. 7. (Color online) (a) Image of the displacement in a fully water-wet porous medium. (b) BLCPS of a segment of the capillary pressure signal representative of the displacement in a water-wet porous medium. (c) Image of the displacement in a strongly oil-wet porous medium. (d) BLCPS of a segment of the capillary pressure signal representative of the displacement in a strongly oil-wet porous medium.

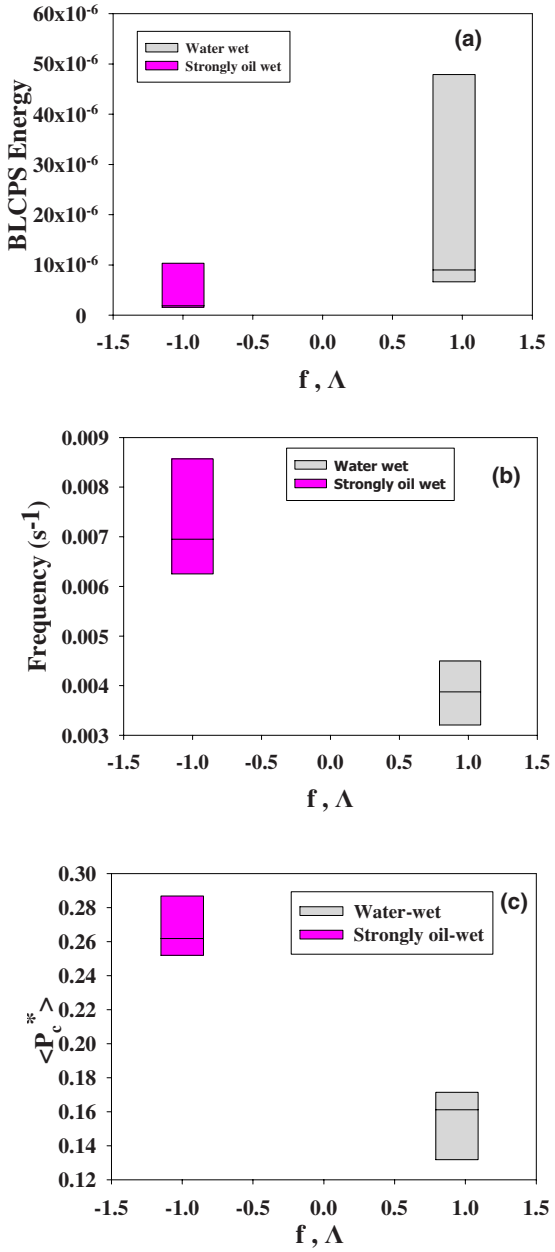

FIG. 8. (Color online) Variance of the (a) BLCPS energy, (b) BLCPS frequency, and (c) time-averaged dimensionless capillary pressure, measured from displacement experiments on water-wet and strongly oil-wet porous media (the horizontal lines indicate the corresponding mean values).

shown in Fig. 6(b). The frontal wettability is defined by

$$\Lambda = f_{ow} \cos \theta_{ow} + f_{ww} \cos \theta_{ww}, \tag{14}$$

where f_{ow} and f_{ww} are the fractions of oil-wet spheres and water-wet spheres at the interface, respectively, θ_{ow} is the contact angle of the fluid system with respect to the oil-wet surface, and θ_{ww} is its contact angle with respect to the water-wet surface. The differences between the two images [Figs. 6(b) and 6(c)] show the area invaded by water at a given time interval [Fig. 6(a)]. The regional wettability of the invaded area f is defined by the index

$$f = f_1 \cos \theta_{ww} + f_2\left(\frac{2}{3}\cos \theta_{ww} + \frac{1}{3}\cos \theta_{ow}\right) + f_3\left(\frac{1}{3}\cos \theta_{ww} + \frac{2}{3}\cos \theta_{ow}\right) + f_4 \cos \theta_{ow}, \tag{15}$$

where f_1 is the fraction of fully water-wet (ww-ww-ww) pores (pores between three glass spheres) invaded, f_2 is the fraction of ww-ww-ow pores (pores between two glass and one PTFE spheres) invaded, f_3 is the fraction of ww-ow-ow pores (pores between one glass and two PTFE spheres) invaded, and f_4 is the fraction of fully oil-wet (ow-ow-ow) pores (pores between three PTFE spheres) invaded. For the POW fluid system, both the frontal, Λ, and regional wettability, f, range from -1 to 0.94, as the pore system becomes from fully oil wet to fully water wet. The index f is an updated version of wettability factor F reported in [36].

VI. RESULTS AND DISCUSSION

A. Displacement in uniformly wet porous media

The transient response of the capillary pressure during oil displacement from a water-wet porous medium ($f=\Lambda=0.94$) [Fig. 7(a)] is characterized by slow fluctuations [Fig. 7(b)] that are isolated at high wavelet levels (fifth and sixth). Compared to the water-wet case, the transient response of capillary pressure measured during a displacement in a strongly oil-wet porous medium ($f=\Lambda=-1.0$) [Fig. 7(c)] is characterized by faster and lower-amplitude fluctuations [Fig. 7(d)] which are isolated at the third or more rarely at the fourth wavelet level.

The BLCPS energy of the water-wet porous medium ($f=\Lambda=0.94$) ranges in a wider domain compared to that of the strongly oil-wet porous medium ($f=\Lambda=-1.0$) [Fig. 8(a)]. The BLCPS frequency of the water-wet porous medium is smaller than that of the oil wet [Fig. 8(b)]. Oil displacement in a water-wet porous medium, follows a compact growth pattern [Fig. 7(a)] because of the small contact angle ($\theta_e=20°$), which favors the interaction of neighboring menisci (interface smoothing) and the formation of a unified interface [43]. Instead, the displacement in the oil-wet porous medium is a ramified growth pattern as the contact angle is very high and the process resembles much more invasion percolation [Fig. 7(c)]. The invading phase (water) in the water-wet porous medium occupies the entire cross section of pores and a late breakthrough is observed. In other words, pore filling is slow resulting in low frequency fluctuations [Figs. 7(b) and 8(b)] associated with a relatively high wavelet best level. In addition, the penetration of large volumes of water in the pores of the water-wet porous medium results in high amplitude fluctuations [Fig. 7(b)] that are associated with high energy values [Fig. 8(a)].

The homogeneity of the spatial distribution of wettability in the water-wet case in combination with the compact growth pattern is reflected in the low frequency of BLCPS [Figs. 7(b) and 8(b)]. This spatial homogeneity is locally disturbed in the oil-wet case by the presence of the water-wet upper and lower surfaces (glass cover plates). In other words, all pores are mixed-wet and hence, the motion of an oil-

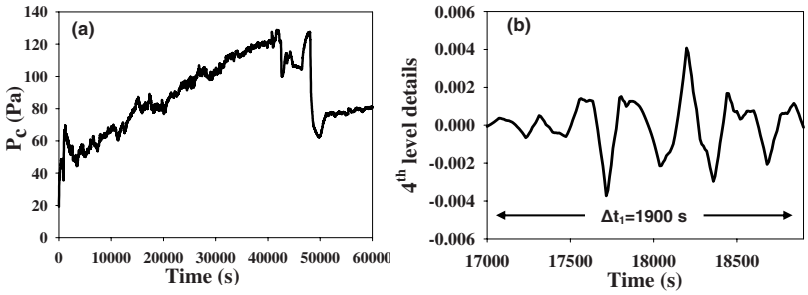

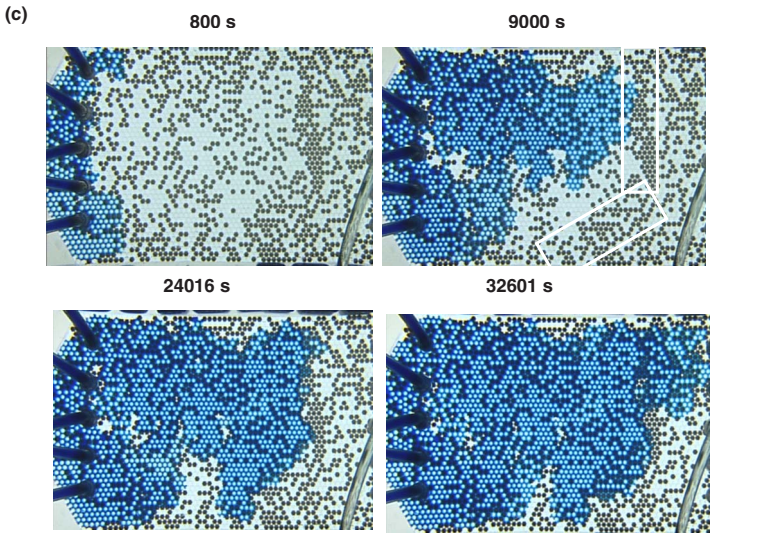

FIG. 9. (Color online) (a) Signal of the capillary pressure measured during water-oil displacement in a porous medium with $\xi = 0.44$ (model A). (b) BLCPS representative of the displacement in model A. (c) Successive snapshots of the displacement in model A.

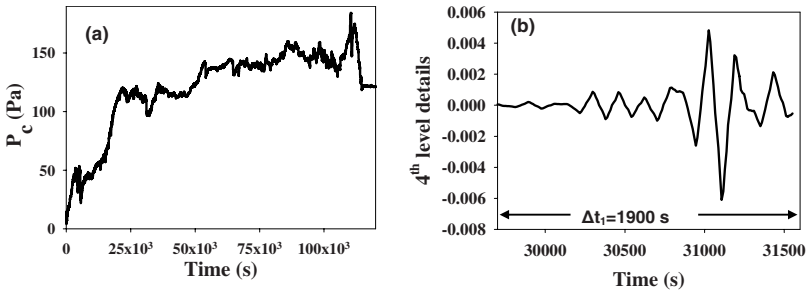

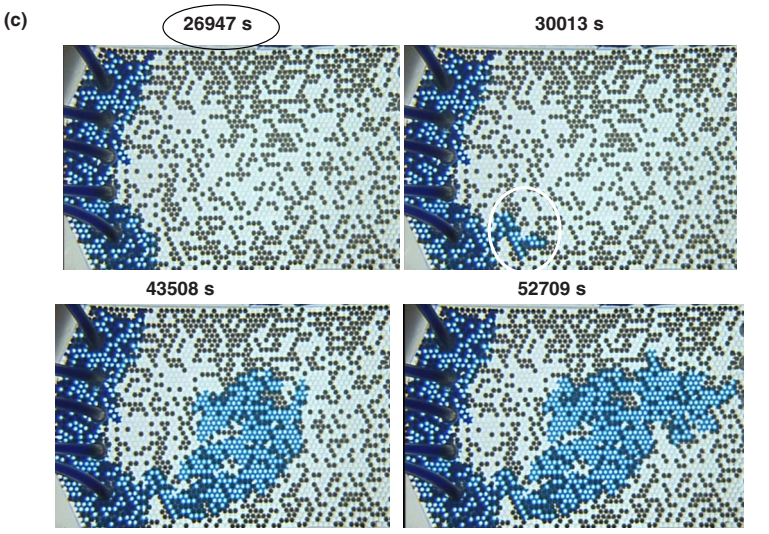

FIG. 10. (Color online) (a) Signal of the capillary pressure measured during water-oil displacement in a porous medium with $\xi = 0.44$ (model B). (b) BLCPS representative of the displacement in model B. (c) Successive snapshots of the displacement in model B.

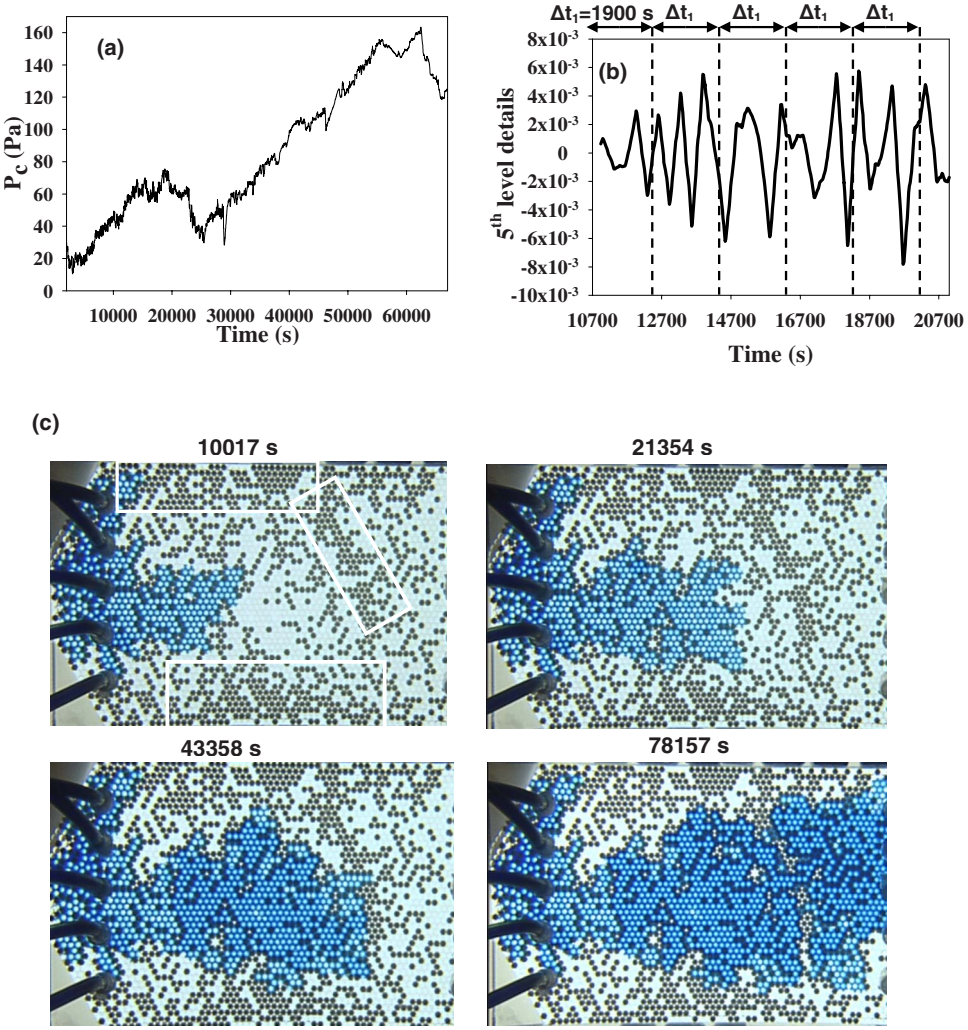

FIG. 11. (Color online) (a) Signal of the capillary pressure measured during water-oil displacement in a porous medium with ξ=0.44 (model C). (b) BLCPS representative of the displacement in model C. (c) Successive snapshots of the displacement in model C.

water meniscus is favored by the water-wet surface and is prevented by the oil-wet surface. The motion along the water-wet surfaces (imbibition with small contact angle) has the tendency to create a compact pattern while the motion through the oil-wet pore boundaries tends to create a fractal percolation cluster [43]. The net effect of these opposite trends is the ramified pattern shown in Fig. 7(c). At the pore level, only a fraction of the pore volume is occupied by water as a significant amount of oil is bypassed and is retained in the oil-wet pore corners. This is confirmed easily at various stages of the displacement, since the cumulative water volume injected (and measured) by the syringe pump is always much less than the total volume of the (visually measured) pores filled with water. Consequently, the water/oil displacement in an oil-wet porous medium evolves as a fast process where the flow from high-curvature regions to low-curvature regions and vice versa takes place very quickly. Consequently, the fluctuations of the capillary pressure signal are fast [Fig. 7(d)] and the best level is relatively low (third or fourth). The oil bypass mechanism is associated with low energy dissipation, and fast flow events are reflected in low BLCPS energy [Fig. 8(a)] and high BLCPS frequency [Fig. 8(b)], respectively.

B. Displacement experiments in fractional wet porous media

1. Displacement experiments at ξ=0.44

At each experiment, the oil-wet and water-wet spheres are distributed randomly in the pack [36]. When considering two sphere-packs of the same fraction of oil-wet spheres, ξ, the spatial distribution of the oil-wet and water-wet spheres will differ from one packing to the other. This difference in spatial distribution of wettability may result in different flow paths of the displacing phase (water) and different capillary pressure signals (Figs. 9–11).

The random distribution of spheres in model porous medium A (Fig. 9) created a continuous chain of oil-wet spheres spanning the network between the two lateral boundaries [Fig. 9(c)]. So, in advanced stages of the displacement, this chain of oil-wet spheres acts as capillary barrier that blocks the frontal motion, and prevents water invasion along the flow direction [Fig. 9(c)]. Under continuous injection, water is forced to invade areas behind the front with the capillary pressure ($P_c \sim 130$ Pa) increasing [Fig. 9(a)] until breakthrough occurs [Fig. 9(c)].

In model porous medium B (Fig. 10) the flow growth pattern differs [Fig. 10(c)] from that of model A [Fig. 9(c)] as the displacing phase (water) follows a flow path dominated

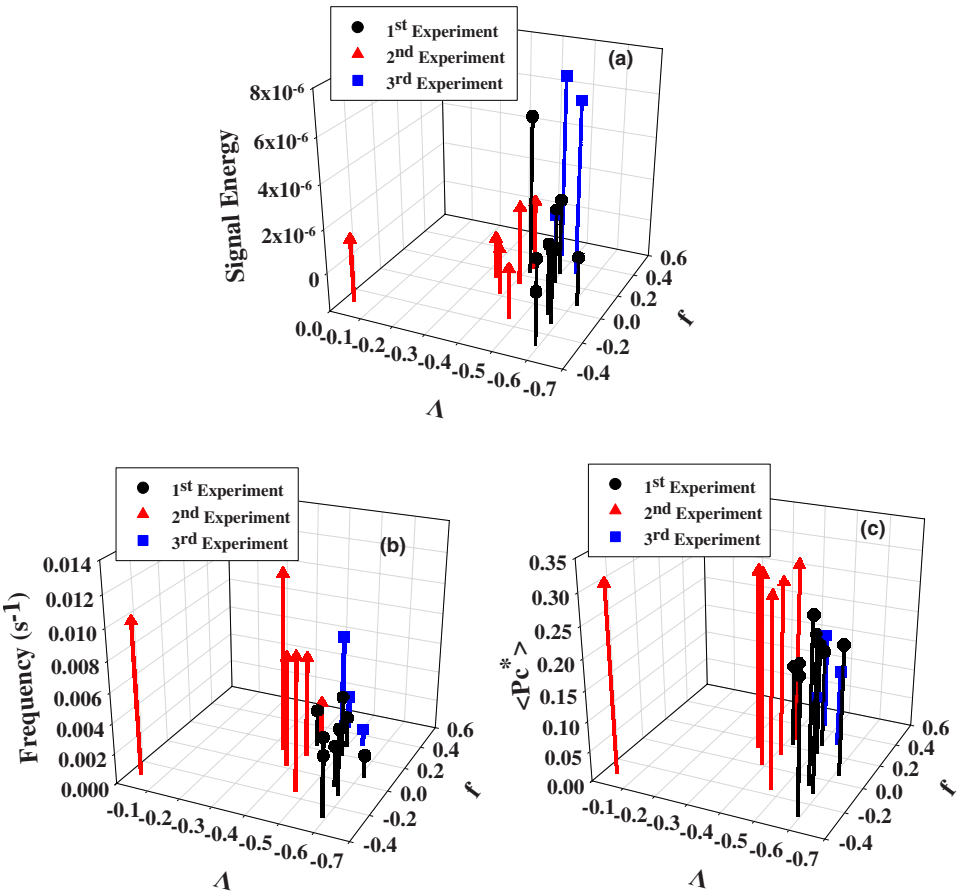

FIG. 12. (Color online) (a) BLCPS energy, (b) BLCPS frequency, and (c) time-averaged dimensionless capillary pressure, versus frontal and regional wettability indices for displacement experiments performed on fractional-wet models A (Fig. 9), B (Fig. 10), and C (Fig. 11) having identical ξ=0.44 but different spatial distributions of wettability.

by water-wet areas surrounded by oil-wet boundaries [Fig. 10(c)]. The capillary pressure fluctuates over a small range [Fig. 10(a)] and the oil recovery efficiency is relatively low [Fig. 10(c)].

Likewise, in model C (Fig. 11) water moves along a flow path dominated by water-wet areas surrounded by oil-wet boundaries [Fig. 11(c)]. However, again a network-spanning cluster of oil-wet spheres blocks the frontal displacement and water starts moving backward by occupying both layers of the pore network as it is revealed by the dark color in Fig. 11(c). The capillary pressure is small enough until frontal displacement is blocked by the oil-wet capillary barrier [Fig. 11(c), $t \approx 40\,000$ s] and increases under an almost constant slope, until overcoming the barrier ($P_c \sim 165$ Pa) [Fig. 11(a)].

The parameters of the capillary pressure signals (BLCPS energy, BLCPS frequency, time-averaged capillary pressure) measured in the foregoing experiments [Figs. 9(a), 10(a), and 11(a)] were determined with the aid of the methodology described in Sec. IV and illustrated in Figs. 4 and 5. From successive snapshots of the displacement growth pattern [Figs. 9(c), 10(c), and 11(c)] the regional and frontal wettability indices were determined. During water invasion in oil-wet pores formed between oil-wet (PTFE) (ow-ow) spheres, most of the oil is bypassed, as preferential flow along the water-wet surfaces (cover glass plates) occurs and each pore becomes occupied by a small amount of water. In mixed-wet (ow-ww) pores, the pore volume fraction occupied by the displacing fluid (water) increases and in water-wet pores (ww-ww) complete filling occurs. As was explained earlier, the advancement of menisci in oil-wet areas will be accompanied by frequent and low-amplitude fluctuations [Fig. 9(b)], while the invasion of water-wet areas is reflected in less frequent and high-amplitude fluctuations [Fig. 10(b)]. An intermediate situation is expected during the invasion of mixed-wet areas [Fig. 11(b)]. It seems that the pattern of BLCPS is a fingerprint of the displacement growth pattern. The amplitude of the fluctuations and hence the BLCPS energy increases as more oil-wet interfaces (low Λ values) are activated and water penetrates into more water-wet areas (high f values) of the porous medium [Fig. 12(a)]. The frequency of the BLCPS seems to increase as fewer oil-wet interfaces (high Λ values) are activated and water invades more oil-wet areas (low f values) of the porous medium [Fig. 12(b)]. The time-averaged capillary pressure increases when oil-wet interfaces (low Λ values) are activated and water invades more oil-wet areas (low f values) of the porous medium [Fig. 12(c)].

2. *Displacement experiments at* ξ=0.59

Displacement experiments were also performed on two model porous media with ξ=0.59 and different spatial variation of water-wet and oil-wet spheres (Figs. 13 and 14).

The oil recovery from model D is high, due to a transverse network spanning cluster of oil-wet spheres that acts as a capillary barrier by preventing water from moving toward the outlets [Fig. 13(c)]. This oil-wet cluster forces water to invade gradually more oil-wet areas which were bypassed

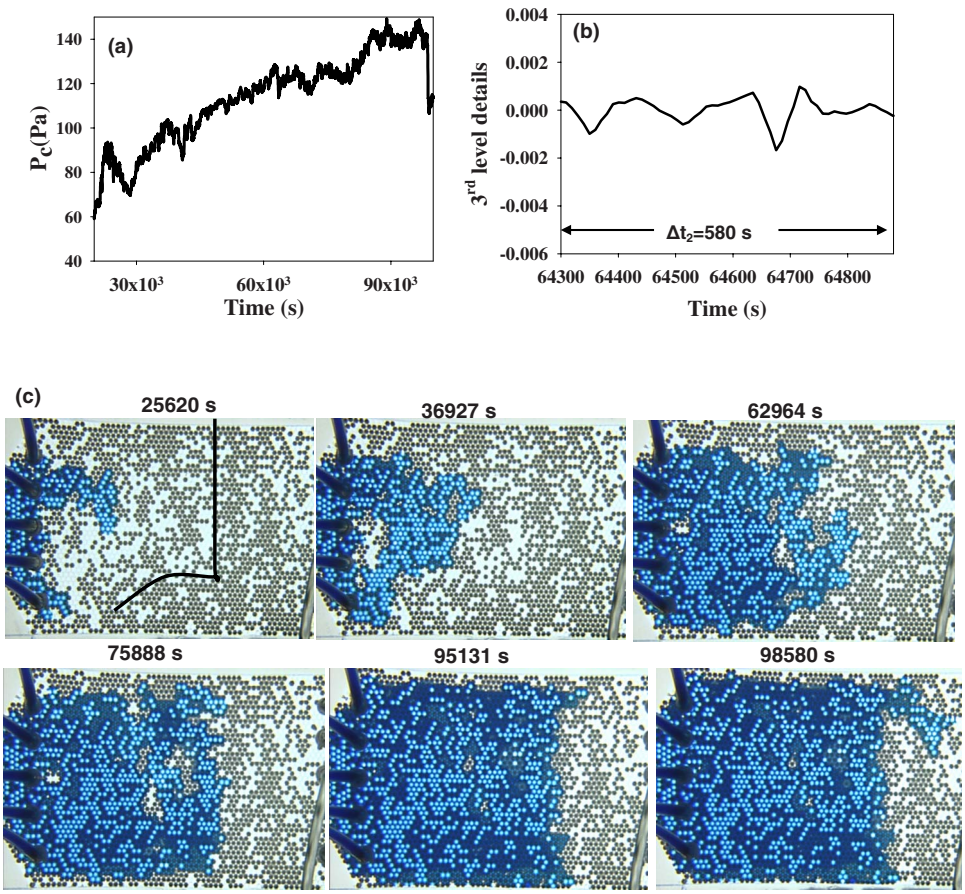

FIG. 13. (Color online) (a) Signal of the capillary pressure measured during water-oil displacement in a porous medium with ξ=0.59 (model D). (b) BLCPS representative of the displacement in model D. (c) Successive snapshots of the displacement in model D.

(including the central area of the invaded oil-wet pores) during injection, and are located behind the displacement front [Fig. 13(c), t=62 964–951 131 s]. The consequence of this backward motion of water is a very compact flow pattern and a high oil recovery efficiency [Fig. 13(c)]. The capillary barrier of the front is overcome at high values of the capillary pressure ($P_c \sim 150$ Pa) where water breakthrough occurs [Figs. 13(a) and 13(c)]. As the displacement grows in oil-wet or mixed-wet areas, the BLCPS fluctuations are characterized by low amplitude [Fig. 13(b)].

Oil-water displacement in model E [Fig. 14(c)] occurs at smaller values of the capillary pressure [Fig. 14(a)] compared to model D. The capillary barrier is overcome at a relatively low value of the capillary pressure ($P_c \sim 105$ Pa), water breakthrough occurs much earlier than in the case of model D, and oil recovery is relatively low [Fig. 14(c)]. With the displacement following water-wet flow paths, the BLCPS fluctuations are characterized by low frequency and high amplitude [Fig. 14(b)].

The main difference between the flow patterns in models D and E is that in the one case (D) water invades oil-wet areas [Fig. 13(c)] whereas in the second case (E) preferential flow along the water-wet flow paths occurs [Fig. 14(c)]. These differences in the flow growth pattern are attributed to the different spatial variation of wettability [Figs. 13(c) and 14(c)] and are reflected in the pattern of BLCPS [Figs. 13(b) and 14(b)].

The amplitude of the BLCPS fluctuations, and hence the BLCPS energy, increases when fewer oil-wet interfaces invade fewer oil-wet areas [Fig. 15(a)]. The frequency of the BLCPS seems to increase as more oil-wet interfaces are activated and fewer oil-wet areas of the porous medium are invaded by water [Fig. 15(b)]. The time-averaged capillary pressure increases when more oil-wet interfaces invade fewer oil-wet areas of the porous media [Fig. 15(c)]. The best levels (BLs) of wavelet analysis is reflected in the frequency of BLCPS fluctuations. The lower the BL, the higher the frequency [Figs. 13(b) and 14(b)]. The best levels are lower (third and fourth) in model D than in model E (fifth). In model D, areas of the porous medium that were bypassed during initial stages of the displacement are invaded when a network spanning cluster of oil-wet spheres blocks the forward motion at the front menisci [Fig. 13(c)]. This backward flow is reflected in low-amplitude fluctuations of BLCPS [Fig. 13(b)]. The displacement in model E is completed in a short period of time and is dominated by less frequent and higher-amplitude fluctuations [Fig. 14(b)] compared to those measured in model D [Fig. 13(b)].

3. Displacement experiments at various ξ values

All data obtained from oil-displacement experiments performed on fractional-wet porous media for various fractions of oil-wet spheres (ξ=0.25,0.44,0.59,0.70) were analyzed from the third to the sixth wavelet level. The time-averaged dimensionless capillary pressure, BLCPS energy, and BLCPS frequency calculated from all experiments were correlated with the regional (f) and frontal (Λ) local wettability indices [Figs. 16(a)–16(c)]. The contour lines of the time-

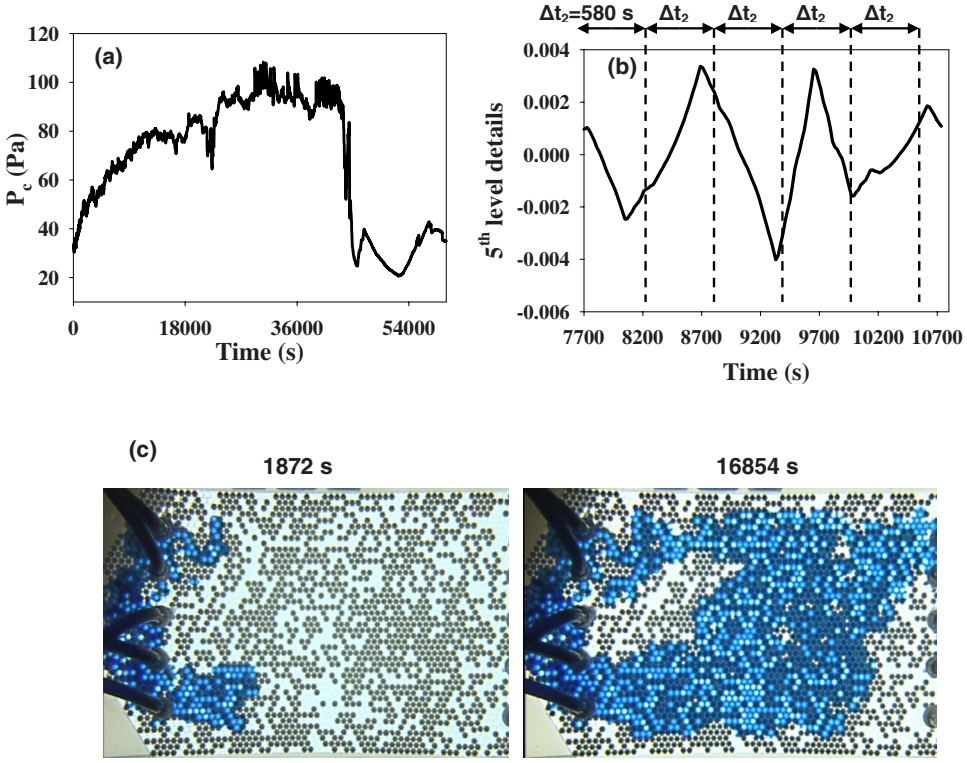

FIG. 14. (Color online) (a) Signal of the capillary pressure measured during water-oil displacement in a porous medium with ξ=0.59 (model E). (b) BLCPS representative of the displacement in model E. (c) Successive snapshots of the displacement in model E.

averaged dimensionless capillary pressure [Fig. 16(a)] show that the capillary pressure increases when the activated interfaces are more oil-wet and water penetrates into more oil-wet areas of the porous medium. Moreover, there is a range of sufficiently low Λ and f values [the valley in contours of Fig. 16(a)] where the capillary pressure takes on low values. This range is attributed to experiments performed at large ξ values where the oil bypass mechanism is dominant.

The BLCPS energy increases when fewer oil-wet interfaces are activated ($\Lambda > -0.2$) and water invades more water-

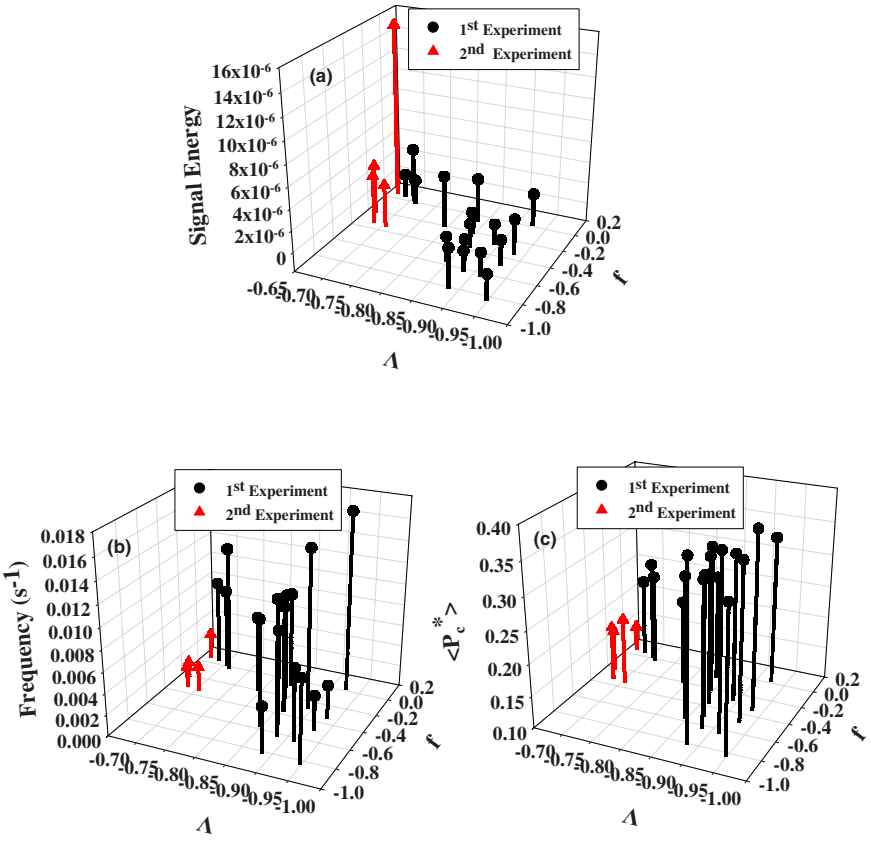

FIG. 15. (Color online) (a) BLCPS energy, (b) BLCPS frequency, and (c) time-averaged dimensionless capillary pressure, versus frontal and regional wettability indices for displacement experiments performed on fractional-wet models D (Fig. 13) and E (Fig. 14) having identical ξ=0.59 but different spatial distributions of wettability.

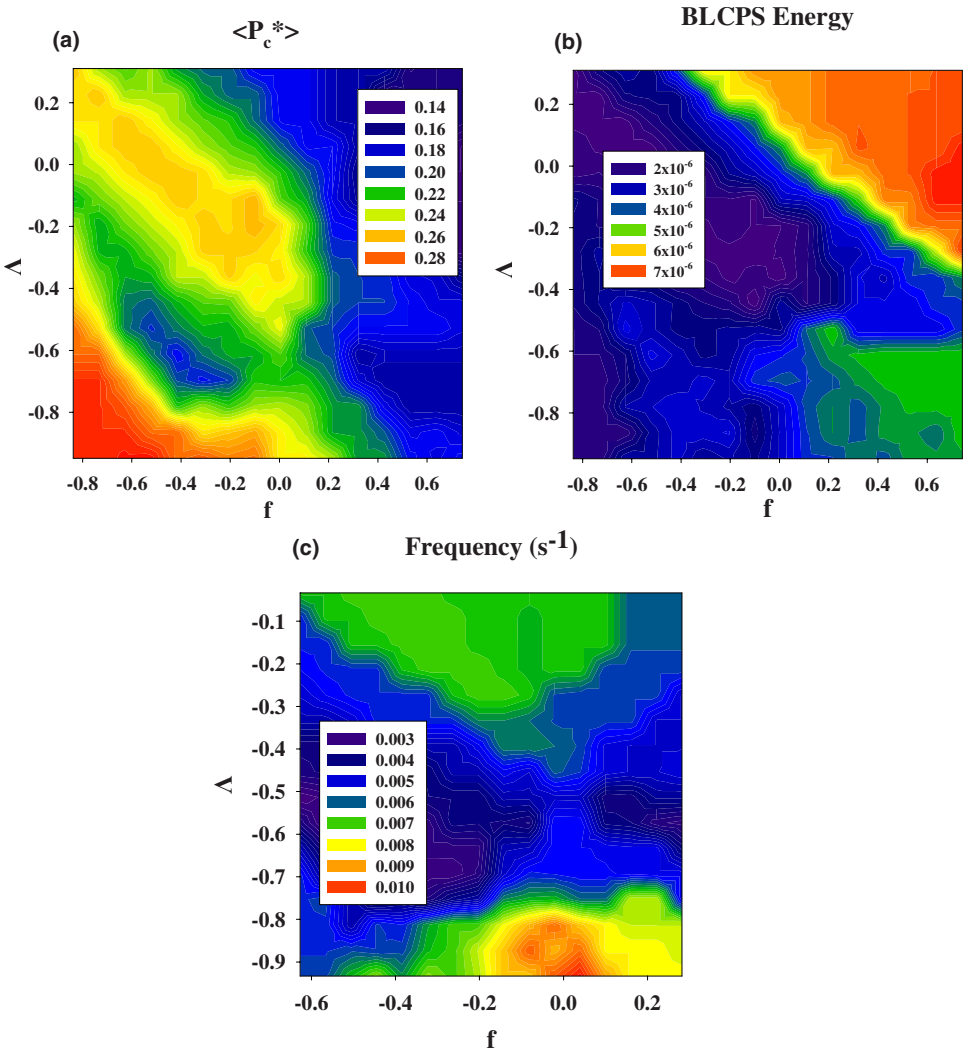

FIG. 16. (Color online) Contours of the (a) time-averaged capillary pressure, (b) BLCPS energy, and (c) BLCPS frequency, calculated from data sets of water-oil displacement in fractional-wet porous media for various values of $\xi=0.25, 0.44, 0.59, 0.70$.

wet areas of the porous medium ($f>0.0$). As the porous medium becomes more water wet, the high amplitude of BLCPS fluctuations is reflected in high energy values [Fig. 16(b)].

The BLCPS frequency [Fig. 16(c)] increases when strongly oil-wet interfaces are activated ($\Lambda<-0.6$) and water invades neutral-wet areas of the porous medium ($-0.3<f<0.3$). This means that many local minima and maxima are observed in the BLCPS when the menisci move from large clusters of oil-wet spheres to mixed-wet areas. The domain of low time-averaged capillary pressures [valley in contour of Fig. 16(a)] is associated with a domain of low BLCPS frequencies [valley in contour of Fig. 16(c)].

4. Capillary pressure calculations

The Mayer and Stowe-Princen-Purcell (MSPP) method [36] was used to estimate the maximum (critical) dimensionless curvature for a meniscus to penetrate into horizontal pore throats (formed between one plate and two spheres) or vertical pore throats (formed between three spheres touching each other) [Fig. 17(a)]. The horizontal throats are penetrated at lower values of "breakthrough" capillary pressure compared to that of vertical throats, and this is an explanation of the fact that in most cases, water prefers to invade one or both layers of the porous medium with the vertical throats being occupied by oil. The time-averaged capillary pressure measured at various ξ values was converted to a dimensionless curvature J^*, by using Fig. 17(a) and the following relation:

$$J^* = J_1^*(\theta_1) f_s + J_2^*(\theta_2)(1 - f_s), \tag{16}$$

where f_s is the oil-wet fraction of the solid surface given by

$$f_s = \xi\left(\frac{\pi}{\sqrt{3}+\pi}\right). \tag{17}$$

The experimentally measured average curvatures diverge from the theoretically predicted ones when the fraction ξ takes on high values [Fig. 17(b)]. When the fraction ξ is large enough ($\xi>0.6$) most of the pores are oil wet. During the motion of water in pores formed between ow-ow spheres, the meniscus tends to move along the water-wet glass plates, whereas the central area of the oil-wet pore remains occupied by oil. The situation becomes much more complicated when a meniscus tends to penetrate into a mixed-wet pore. Such "heterogeneous" interfacial configurations are unable to be simulated by the approximate MSPP method [36] with the

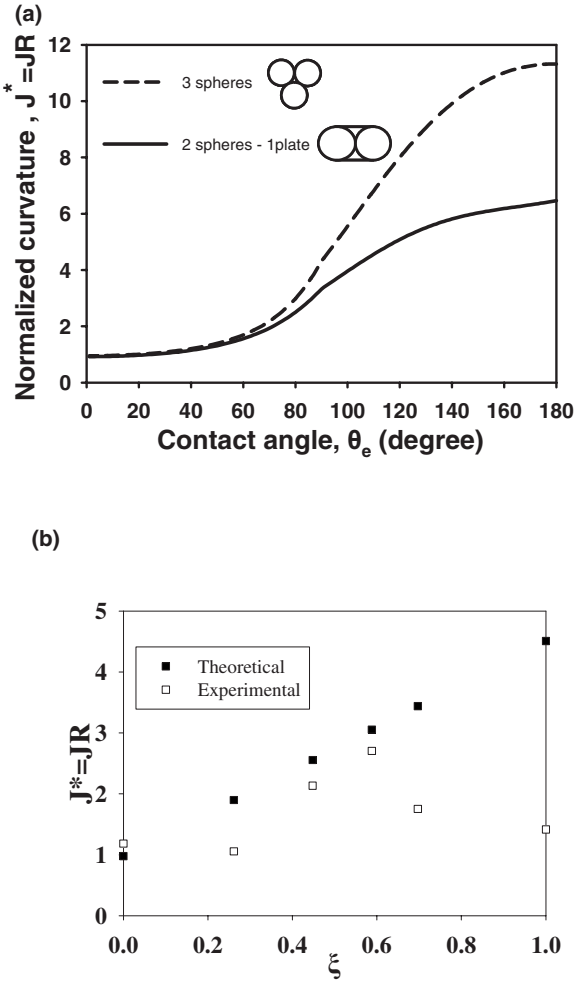

FIG. 17. (a) Critical (maximum) curvature for a meniscus penetration into a pore enclosed between either one plate and two spheres or three spheres (the calculation was based on the MSPP method). (b) Comparison of approximate theoretical predictions based on (a) and Eq. (16) with prebreakthrough time-averaged dimensionless meniscus curvature calculated from capillary pressure signals measured during displacement experiments on fractional-wet porous media.

result that a discrepancy between theory and experiment arises [Fig. 17(b)].

VII. CONCLUSIONS

The aim of this work is twofold: (1) to present a robust method for the wavelet analysis of the capillary pressure signals measured during rate-controlled displacement experiments in porous media, and (2) to correlate properties of the signals analyzed with wavelets (CPS) to quantitative measures of the spatial variation of wettability over the porous medium.

Immiscible displacement visualization experiments were performed on fractional-wet model packings consisting of strongly oil-wet and water-wet spheres by using the paraffin oil (defender)–water (invader) system. Analyzing with wavelets the measured signal of the capillary pressure up to the level where the entropy of the approximation approaches zero allows us to get the best level capillary pressure spectrum (BLCPS) which still contains the maximum information about the original signal. The BLCPS energy and frequency of fluctuations along with the time-averaged capillary pressure quantify the signal of capillary pressure and change with time as the displacement proceeds. Video-recorded images of the displacement allow us to calculate two wettability indices that quantify the spatial variation of wettability of the invaded areas of the porous medium: (1) the frontal wettability of the active interface (front) before an invasion step taking place, and (2) the regional wettability of the area invaded by the displacing fluid.

When analyzing a capillary pressure signal with wavelets, the best level provides information about the duration of the capillary pressure fluctuations, and consequently for the duration of the flow events that take place during the displacement. In a fractional-wet pore system, the more oil-wet the area invaded, the faster the flow events, and the faster and smaller (lower amplitude) the fluctuations, the less the pore volume fraction occupied by the invader (water). The more the water-wet area invaded, the slower and larger (higher amplitude) the fluctuations, and the greater the pore volume fraction occupied by the invader. The best level of wavelet analysis is low in the case of strongly oil-wet porous media (fast fluctuations) and high in the case of water-wet porous media (slow fluctuations). In general, the BLCPS energy decreases and the BLCPS frequency increases as the pore system becomes more oil wet.

When considering fractional-wet porous media, the spatial variation of the oil-wet and water-wet surfaces over the porous medium is of key importance for the displacement growth pattern and displacement efficiency. Even when the total wettability of the porous medium (expressed by the ratio of oil-wet surface to the total surface) remains identical, the signal of capillary pressure is not unique since the spatial distribution of oil-wet and water-wet surfaces change. The BLCPS energy, which is an increasing function of the amplitude of the fluctuations and representative of the energy of the original signal, increases as fewer oil-wet interfaces are activated and water invades more water-wet areas. The BLCPS frequency, which is representative of the frequency of the most important fluctuations of the original signal, increases when strongly oil-wet interfaces are activated and water invades water-wet areas of the porous medium. The compact (frontal) flow growth pattern in a water-wet porous medium is accompanied by high-amplitude and low-frequency fluctuations (Table III). The bypass mechanism which prevails in displacements in strongly oil-wet porous media is accompanied by low-amplitude and high-frequency fluctuations (Table III). When the displacement is blocked by oil-wet clusters that span the network in a direction transverse to the main flow, then the backward flow to progressively more oil-wet areas results in high-frequency and low-amplitude fluctuations of the BLCPS (Table III). If the displacement is not blocked but follows water-wet flow paths, bypassing most of the oil contained in individual pores of the pore network, then low-frequency and high-amplitude fluctuations of the BLCPS arise (Table III). The above described patterns of BLCPS are quantified by the energy and

TABLE III. BLCPS parameters and prevailing displacement mechanisms.

BLCPS Parameters / Displacement mechanism	Energy	Frequency	Level
Compact flow (water-wet)	High	Low	High
Bypass (strongly oil-wet)	Low	High	Low
Bypass (fractional-wet)	High	High	High
Backward displacement behind the front menisci when an oil-wet chain blocks the forward motion.	Low	High	Low

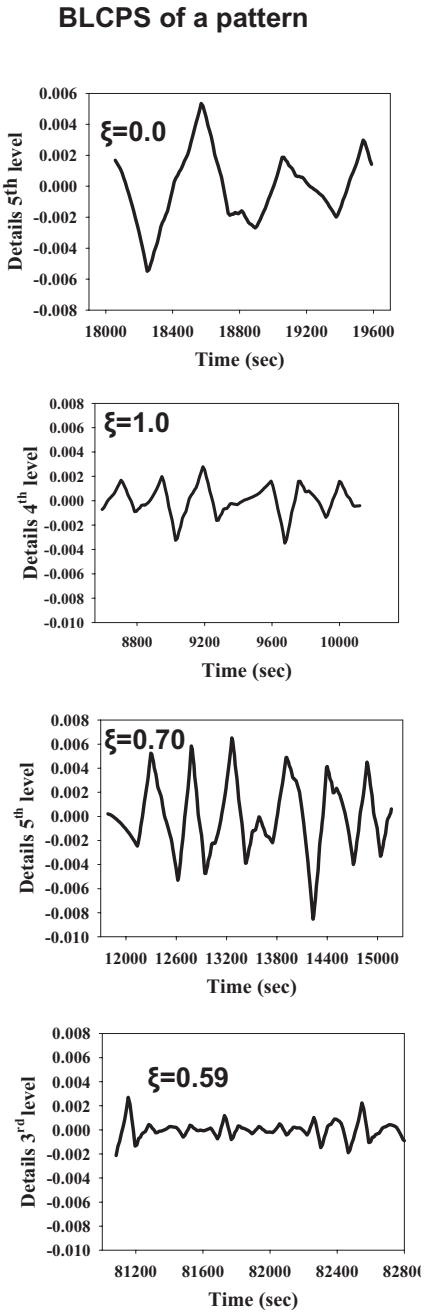

frequency and could be combined with pattern recognition algorithms to provide quantitative information about the spatial variation of wettability in a porous medium.

ACKNOWLEDGMENTS

The present work was supported by the European Commission (Sixth Framework Program, Thematic Area: "Global Change and Ecosystems"), Contract No. SSPI-CT-2003-004017-STRESOIL.

APPENDIX A: MULTISCALE WAVELET ANALYSIS

One discrete time signal $x(t)$ can be analyzed by using discrete wavelet transform defined by [44]

$$W_{j,k} = \int_{-\infty}^{\infty} x(t)\psi^*(t)dt,$$

where $\psi^*(t)$ is the complex conjugate of the wavelet function $\psi(t)$:

$$\psi_{j,k}(t) = 2^{j/2}\psi(2^j t - k),$$

where the integer j is the scale factor and the integer k is a translation factor. When a signal is analyzed by using a wavelet function, the signal passes through two filters and emerges as two signals. The low-pass filter gives the approximations that are the high-scale, low-frequency compo-

nents of the original signal and the approximation coefficients are described by

$$S_{j,k} = \int_{-\infty}^{\infty} x(t)\phi_{j,k}(t)dt,$$

where $\phi_{j,k}(t)$ is the scale function defined by

$$\phi_{j,k} = 2^{-1/2}\phi(2^{-j}t - k).$$

The approximation signal is given by the sum of the scale functions multiplied by the approximation coefficients:

$$x_j(t) = \sum_{k=-\infty}^{\infty} S_{j,k}\phi_{j,k}(t),$$

whereas the detail signal arises from the wavelet coefficients:

$$d_j(t) = \sum_{k=-\infty}^{\infty} W_{j,k}\psi_{j,k}(t).$$

The wavelet analysis of a signal can be extended to more than one level by analyzing the previous approximation signal.

The original signal $x(t)$ can be described by the approximation and detail coefficients

$$x(t) = \sum_{k=-\infty}^{\infty} S_{j_0,k}\phi_{j_0,k}(t) + \sum_{j=-\infty}^{\infty}\sum_{k=-\infty}^{\infty} W_{j,k}\psi_{j,k}(t),$$

i.e., the original signal can be described by one combination of the approximation at an arbitrary scale j_0 enhanced by a sequence of signal details at all the scales.

APPENDIX B: SIGNAL ENERGY

Supposing we have two Riemann integrable complex functions $A(t)$ and $B(t)$ at a radius R of period 2π with Fourier sequences [45], $\Sigma_{n=-\infty}^{\infty} a_n e^{\text{int}}$ and $\Sigma_{n=-\infty}^{\infty} b_n e^{\text{int}}$, respectively, then

$$\sum_{n=-\infty}^{\infty} a_n\overline{b_n} = \frac{1}{2\pi}\int_{-\pi}^{\pi} A(t)\overline{B(t)}dt,$$

where the horizontal bars define the complex conjugation. When $A=B$,

$$\sum_{n=-\infty}^{\infty} |a_n|^2 = \frac{1}{2\pi}\int_{-\pi}^{\pi} |A(t)|^2 dt.$$

The Parseval theorem in physics and engineering is described by

$$\int_{-\infty}^{\infty} |f(t)|^2 dt = \int_{-\infty}^{\infty} |X(f)|^2 dt,$$

where $X(f)=F\{f(t)\}$ is the continuous Fourier transform of the function $f(t)$. For discrete time signals the Parseval theorem is described by

$$\sum_{n=-\infty}^{\infty} |f[n]|^2 = \frac{1}{2\pi}\int_{-\pi}^{\pi} |F(e^{j\phi})|^2 d\phi,$$

where F is the discrete time Fourier transform of the function f and ϕ is the angle frequency of f. Alternatively, for discrete Fourier transform the above equation becomes

$$\sum_{n=0}^{N-1} |f[n]|^2 = \frac{1}{N}\sum_{k=0}^{N-1} |F[k]|^2,$$

where $F[k]$ is the discrete Fourier transform of $f(n)$, both of length N.

[1] G. J. Hirasaki, SPERE **6**, 217 (1991).
[2] L. E. Cuiec, *Evaluation of reservoir wettability and its effects on oil reservoir*, in Interfacial Phenomena in Oil Recovery, edited by N. R. Morrow (Marcel Dekker, New York, 1990), p. 319.
[3] P. P. Jadhunandan and N. R. Morrow, SPERE **10**, 46 (1995).
[4] L. L. Schramm and K. Mannhardt, J. Pet. Sci. Eng. **15**, 101 (1996).
[5] C. M. Odlenburg, K. Pruess, and S. M. Benson, Energy Fuels **15**, 293 (2001).
[6] W. G. Anderson, JPT, J. Pet. Technol. **38**, 1125 (1986).
[7] A. R. Kovscek, H. Wong, and C. J. Radke, AIChE J. **39**, 1072 (1993).
[8] C. Laroche, O. Vizika, and F. Kalaydjian, J. Pet. Sci. Eng. **24**, 155 (1999).
[9] J. M. Schembre, G.-Q. Tang, and A. R. Kovscek, J. Pet. Sci. Eng. **52**, 131 (2006).
[10] C. Shin and G. G. Chase, AIChE J. **50**, 343 (2004).
[11] C. Lim and C. Y. Wang, Electrochim. Acta **49**, 4149 (2004).
[12] A. Z. Weber, R. M. Darling, and J. Newman, J. Electrochem. Soc. **151**, A1715 (2004).
[13] J. T. Gostick, M. W. Fowler, M. A. Ioannidis, M. D. Pritzker, Y. M. Volfkovich, and A. Sakars, J. Power Sources **156**, 375 (2006).
[14] Th. Groth, G. Altankov, and K. Klosz, Biomater Med. Devices Artif. Organs **15**, 423 (1994).
[15] S. A. Bradford and F. J. Leij, J. Contam. Hydrol. **20**, 89 (1995).
[16] D. M. O'Carroll, L. M. Abriola, C. A. Polityka, S. A. Bradford, and A. H. Demond, J. Contam. Hydrol. **77**, 247 (2005).
[17] S. W. Woods, A. Birkas, and R. Ahl, Geomorphology **86**, 465 (2007).
[18] S. H. Doerr, R. A. Shakesby, W. H. Blake, C. J. Chafer, G. S. Humphreys, and P. J. Wallbrink, J. Hydrol. **319**, 295 (2006).
[19] W. G. Anderson, JPT, J. Pet. Technol. **38**, 1246 (1986).
[20] A. B. Dixit, J. S. Buckley, S. R. McDougall, and K. S. Sorbie, Transp. Porous Media **40**, 27 (2000).
[21] A. Dominguez, H. Perez-Aguilar, F. Rozas, and I. Kornhauser, Colloids Surf., A **187-188**, 415 (2001).
[22] S. H. Al-Mahrooqi, C. A. Grattoni, A. K. Moss, and X. D. Jing,

J. Pet. Sci. Eng. **39**, 389 (2003).
[23] S. H. Al-Mahrooqi, C. A. Grattoni, A. H. Muggeridge, R. W. Zimmerman, and X. D. Jing, J. Pet. Sci. Eng. **39**, 389 (2003).
[24] K. Taumer, H. Stoffregen, and G. Wessolek, Geoderma **125**, 107 (2005).
[25] C. P. Morley, K. A. Mainwaring, S. H. Doerr, P. Douglas, C. T. Lewllyn, and L. W. Dekker, Austral. J. Soil Res. **43**, 239 (2005).
[26] W. H. Blake, I. G. Droppo, S. H. Doerr, G. S. Humphreys, R. A. Shakesby, and P. J. Wallbrink, J. Geophys. Res. **112**, F02020 (2007).
[27] L. Zhai, M. C. Berg, F. C. Cebeci, Y. Kim, J. M. Milwid, M. F. Rubner, and R. E. Cohen, Nano Lett. **6**, 1212 (2006).
[28] V. Zorba, L. Persano, D. Pisignano, A. Athanassiou, E. Stratakis, R. Cingolani, P. Tzanetakis, and C. Fotakis, Nanotechnology **17**, 3234 (2006).
[29] M. W. Cao, X. Y. Song, J. Zhai, J. B. Wang, and Y. L. Wang, J. Phys. Chem. B **110**, 13072 (2006).
[30] Z. J. Zheng, O. Azzaroni, F. Zhou, and W. T. S. Huck, J. Am. Chem. Soc. **128**, 7730 (2006).
[31] T. Traykova, C. Aparicio, M. P. Ginebra, and J. A. Planell, Nanomedicine **1**, 91 (2006).
[32] C. D. Tsakiroglou and M. Fleury, J. Pet. Sci. Eng. **22**, 253 (1999).
[33] E. Aker, K. J. Maloy, and A. Hansen, Phys. Rev. E **58**, 2217 (1998).
[34] E. Aker, K. J. Maloy, A. Hansen, and G. G. Batrouni, Transp. Porous Media **32**, 163 (1998).
[35] A. Riaz, G.-Q. Tang, H. A. Tchelepi, and A. R. Kovscek, Phys. Rev. E **75**, 036305 (2007).
[36] V. Sygouni, C. D. Tsakiroglou, and A. C. Payatakes, Phys. Fluids **18**, 053302 (2006).
[37] G. Mason and N. R. Morrow, J. Colloid Interface Sci. **168**, 130 (1994).
[38] J. L. Hilden and K. P. Trumble, J. Colloid Interface Sci. **267**, 463 (2003).
[39] S. K. Starrett, Electr. Power Syst. Res. **38**, 199 (1997).
[40] G. G. Katul, M. B. Parlange, and C. R. Chu, Phys. Fluids **6**, 2480 (1994).
[41] G. G. Katul and M. B. Parlange, Boundary-Layer Meteorol. **75**, 81 (1995).
[42] D. Labat, J. Hydrol. **314**, 275 (2005).
[43] N. Martys, M. O. Robbins, and M. Cieplak, Phys. Rev. B **44**, 12294 (1991).
[44] I. Daubechies, *The Lectures on Wavelets* (SIAM, Philadelphia, 1992).
[45] M. Izumi and S-I. Izumi, J. Math. Anal. Appl. **18**, 252 (1967).
[46] C. E. Shannon, Bell Syst. Tech. J. **27**, 379 (1948).